lubricants

MDPI

Article

Dynamic Analysis and Control Compensation of the Large Optical Mirror Processing Parallel Robot Considering Motion Pair Friction

Hao Liu [1], Zujin Jin [1,2,*] and Zixin Yin [1,2]

[1] School of Mechanical and Electronic Engineering, Suzhou University, Suzhou 234000, China; lb20050011@cumt.edu.cn (H.L.); yinzixin@ahszu.edu.cn (Z.Y.)
[2] Suzhou University Technology and Research Center of Engineering Tribology, Suzhou University, Suzhou 234000, China
* Correspondence: jinzj@ahszu.edu.cn

Abstract

The dynamic performance of parallel robots directly determines the machining accuracy in large optical mirror processing (LOMP). However, limitations in traditional dynamic modeling methods hinder their application in real-time control, constraining further improvements in robotic precision. This paper aims to establish a high-precision and practical dynamic model that considers joint friction for parallel robots used in LOMP, and to design an efficient real-time friction compensation control strategy to effectively enhance trajectory tracking and repetitive positioning accuracy. The novelty of this work lies in proposing a dynamic modeling approach that integrates the static mechanics-based "Disassembly Method" with a "Coulomb + Viscous" friction model. First, static analysis of the mechanism is conducted using the "Disassembly Method" to accurately compute the joint constraint reactions in any pose, providing critical input for friction calculation. Subsequently, a complete dynamic model incorporating friction in joints such as Hooke joints, composite spherical hinges, and ball screws is developed based on the Newton–Euler formulation. This method overcomes the shortcomings of traditional approaches in solving joint reactions and managing model complexity. Numerical simulations demonstrate that, compared to conventional friction-neglected models, the proposed model reveals a maximum increase of approximately 350 N in driving chain joint reaction forces and significant peaks in driving forces at motion reversal instants (e.g., 0.28 s, 0.45 s), quantitatively proving that neglecting friction severely underestimates the actual system loads. Experimental validation shows that the feedforward PD friction compensator designed based on this model reduces the rotational tracking errors of the moving platform around the *X*- and *Y*-axis from 0.295° and 0.286° to 0.134° and 0.128°, respectively, achieving an error reduction of about 55% and effectively improving motion control accuracy. This study provides a reliable dynamic modeling foundation and an effective real-time control compensation solution to address force output errors and trajectory deviations caused by joint friction in high-precision LOMP.

Keywords: parallel mechanism; Newton–Euler method; dynamic modeling; kinematic pair friction; feedforward PD control; friction compensation

check for updates

Received: 9 October 2025
Revised: 10 November 2025
Accepted: 16 November 2025
Published: 18 November 2025

Citation: Liu, H.; Jin, Z.; Yin, Z. Dynamic Analysis and Control Compensation of the Large Optical Mirror Processing Parallel Robot Considering Motion Pair Friction. *Lubricants* **2025**, *13*, 504. https://doi.org/10.3390/lubricants13110504

Copyright: © 2025 by the authors. Licensee MDPI, Basel, Switzerland. This article is an open access article distributed under the terms and conditions of the Creative Commons Attribution (CC BY) license (https://creativecommons.org/licenses/by/4.0/).

1. Introduction

At present, CNC machine tools and series robot are frequently used in the processing of optical mirrors [1]. However, the CNC machine tool, though with a large working stiffness, is inefficient and unable to process the special-shaped surface. The series robot, though with higher dexterity than the CNC machine tool, conducts less accurate repetitive positioning, and the machining process needs many iterations [2]. Additionally, in the process of machining, the large optical mirror surface must be frequently removed from the processing table to test the surface shape and then be relocated and installed. If the repeated positioning is not accurate enough, it will undermine the molding accuracy of the mirror surface. With high stiffness, high motion precision, and high bearing capacity, the parallel robot is widely employed in the situations involving high speed [3], high-precision motion [4], and large loads [5]. Parallel robots present a viable alternative that can overcome the drawbacks associated with CNC machine tools.

In LOMP, the material removal function is directly governed by the normal pressure and relative velocity at the polishing point. Meanwhile, factors including robotic structural parameters, motion patterns, pressure application methods, tool size, and eccentric offset critically influence the proportionality constant of the removal function, thereby collectively determining the system's removal characteristics, operational efficiency, and final accuracy. Notably, the grinding path is directly dictated by the robot's trajectory, while the polishing pressure is subject to the robot's motion accuracy and repeatability. In recent years, to meet the needs of national defense and military and other related fields, large optical mirrors have been transformed from a revolving surface to a profile surface. As a result, the parallel robot demonstrates a more complicated motion curve in the special-shaped surface processing, which cannot even use functions to express. And, the dynamic load produced in the working process is difficult to analyze [6]. Moreover, the parallel robot is easily disturbed by factors like air, temperature, and vibration, thus increasing the difficulty in controlling it and lowering its machining accuracy [7]. So, dynamic control is needed to improve the control precision of the parallel robot. And, combined with the statics analyzed, a dynamic model considering the friction of the robot's motion pair is able to calculate the joint counter force and the driving force of the driving chain under the arbitrary attitude of the parallel robot [8–10]. It is particularly important for the application of parallel robots in LOMP.

Commonly used dynamic modeling methods of parallel mechanisms include Newton–Euler [11], Lagrange [12], virtual work principle [13], Kane equation [14], and improved and combined methods based on the above four methods. Chen et al., incorporating joint clearances to analyze their influence on the system's dynamic behavior, achieved the expected results [15]. Cheng et al., based on the Kane equation, developed a dynamic mechanical model of the hip joint test with a 3SPS + 1PS parallel robot as the core module and applied it to analyze the driving force and dynamic force of the active branch and the restraining reaction of the middle branch [16]. Lang et al. established a flexible multi-body dynamic model of elastic linkages with clearances based on FMD theory [17]. Chen et al. proposed a new scheme of Stewart platform modeling based on the transfer matrix method [18]. Danaei et al. had established a dynamic model by using the principle of virtual work and the concept of the Jacobian matrix. By determining the parameters for basic inertia, a simplified dynamic model was obtained [19]. Hou et al. established a dynamic formula of the Newton–Euler equation to analyze the influence of the hinge clearance on the dynamic characteristics [20]. Jiang et al. established a dynamic model of a cable-driven flexible mechanism by combining the modal method with the Lagrange equation [21]. Yang et al. used the Kane equation to derive the complete inverse dynamic equation of a 6-DOF micro vibration simulator [22]. Wang et al. established a dynamic

model considering the gap of a spherical hinge [23]. The above scholars have completed the dynamic modeling of the research object through different or improved dynamic modeling methods, and obtained certain conclusions. However, there are still some defects in the modeling process. For example, the dynamics modeling is performed using the principle of virtual work. Although the binding force and the joint inertia expression are eliminated, and the calculation efficiency is high in the calculation process, the influence of the motion pair friction on the system is not considered. Moreover, the force of the fulcrum of each member cannot be calculated, and the accuracy of the solution result also cannot be guaranteed [24]. The Lagrange dynamics solving process is cumbersome and computationally intensive, and when considering the motion pair friction, the constructed dynamic model is more complicated and more difficult to solve [25]. The Kane equation and other methods also have the disadvantages of not being able to solve the reaction forces of the joints of the robot during movement [26]. It is difficult to study and analyze the further friction compensation of the organization.

In terms of the robot's control strategy, Van et al. put forward a fast terminal sliding mode control on the basis of adaptive backstepping nonsingular control [27]. Wu et al. proposed a hybrid forces/position control strategy and conducted experiments on a new type of slender and flexible tendon sheath-driven rescue manipulator, thereby adjusting the displacement and clamping forces of the gripper during operation [28]. Considering the fast finite time consistency of distribution of bounded perturbation systems by multiple agents, Nair et al. proposed a robust finite-time event triggering control strategy. The nonlinear consistency protocol they put forward can achieve the required relative state deviation between agents through directed graph topology [29]. Based on industrial rolling mills, Prinz et al. proposed two different automatic gain control methods, and then based on this, they designed a feedforward method for the lateral asymmetry of the inlet thickness profile, verifying the benefits of combining the automatic gain control and feedforward controller to compensate for the asymmetry [30]. Mao et al. proposed a lag compensation method for the positioning accuracy problem, and combined with a feedforward control scheme, they also brought forward a hybrid feedforward controller to correct the model input, realizing hybrid control that combines the feedforward and feedback [31]. Although the control strategy used by the above scholars realizes the motion control of the corresponding robot, the computational burden is large for the designed LOMP robot, which increases instability during the robot's movement. With feedforward PD control, the desired attitude of the robot is first calculated, which can reduce the computational time-consuming burden of the controller.

In summary, while existing research has made significant progress in the dynamic modeling and control of parallel mechanisms, distinct limitations persist when applying these approaches to the specific high-precision context of LOMP. These limitations are primarily manifested in the following two aspects. (1) Disconnect between modeling accuracy and practical utility. Classical methods such as the principle of virtual work and the Lagrangian formulation can establish dynamic models, but they possess inherent shortcomings in handling joint friction. They either completely neglect friction (e.g., the principle of virtual work), leading to significant prediction inaccuracies in low-speed, high-precision machining processes, or they introduce friction at the cost of excessive model complexity and computational difficulty (e.g., the Lagrangian method), hindering their application in real-time control. More critically, these methods generally fail to accurately solve for the joint constraint reactions within the limbs, which are essential inputs for calculating friction forces. Consequently, friction compensation strategies based on such models lack a precise foundation. (2) Conflict between control strategy sophistication and real-time performance. Existing advanced control strategies (e.g., various sliding

mode controls, intelligent controls), while powerful, often involve complex algorithms and heavy computational loads. For the multi-degree-of-freedom, high-dynamic-response parallel robot machining system studied here, overly complex controllers may introduce computational delays, compromising real-time performance and stability.

To overcome these challenges, this paper integrates the static mechanics-based "Disassembly Method of Static Mechanics" with a "Coulomb + Viscous" friction model. Firstly, static analysis is employed to precisely compute the joint reaction forces in any given pose, providing the necessary prerequisite for accurate friction calculation. Subsequently, a complete dynamic model incorporating friction is constructed on this basis. This approach remedies the deficiency of traditional methods (like the principle of virtual work) in determining joint reactions and, while ensuring model accuracy, avoids the complexity issues associated with methods like the Lagrangian formulation when friction is introduced. Addressing the real-time requirements of optical machining, this paper designs a feedforward-based PD friction compensator grounded in the aforementioned high-precision dynamic model. The core of this strategy lies in utilizing the model to pre-calculate frictional disturbances and cancel them out through the feedforward channel. This method offers high computational efficiency and ease of implementation, making it more suitable for industrial machining scenarios requiring prolonged stable operation. The research methodology and technical roadmap of this paper are illustrated in Figure 1.

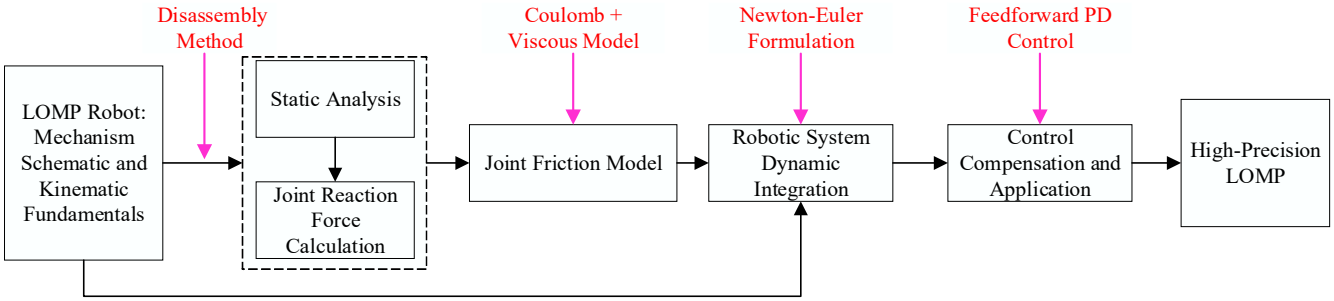


Figure 1. Research methodology and technical roadmap.

2. Kinematic Analysis

The prototype and topology diagram of the LOMP robot are shown in Figure 2a,b, respectively. α, β, and γ are used to represent the RPY angle of the moving platform *o-uvw* with respect to x, y, z in the fixed coordinate system *O-XYZ*, and the attitude vector can be expressed as $\boldsymbol{q} = (\alpha, \beta, \gamma)^{\mathrm{T}}$. The relationship between $\boldsymbol{q}$ and the angular velocity $\boldsymbol{\omega}$ is given by Equation (1).

$$\begin{cases} \boldsymbol{\omega} = \boldsymbol{E} \cdot \dot{\boldsymbol{q}} \\ \dot{\boldsymbol{\omega}} = \boldsymbol{E} \cdot \ddot{\boldsymbol{q}} + \dot{\boldsymbol{E}} \cdot \dot{\boldsymbol{q}} \end{cases} \tag{1}$$

where $\boldsymbol{E} = \begin{pmatrix} c\beta c\gamma & -s\gamma & 0 \\ c\beta s\gamma & c\gamma & 0 \\ -s\beta & 0 & 1 \end{pmatrix}$ (simplified representation of $s\beta = \sin\beta$, $c\beta = \cos\beta$ is applied in the formula).

The closed-loop vector of the limb $\mathrm{B}_i\mathrm{A}_i$ is given by Equation (2).

$$l_i = \boldsymbol{R} \cdot \boldsymbol{a}_i + \boldsymbol{P} - \boldsymbol{b}_i \tag{2}$$

where l_i is the length of the branched $\mathrm{B}_i\mathrm{A}_i$, $\boldsymbol{R}$ is the attitude matrix of the *o-uvw* relative to *O-XYZ*, $\boldsymbol{a}_i$ and $\boldsymbol{b}_i$ are the position vectors of the point A_i and B_i, and $\boldsymbol{p}$ is the position vector of the moving platform center.

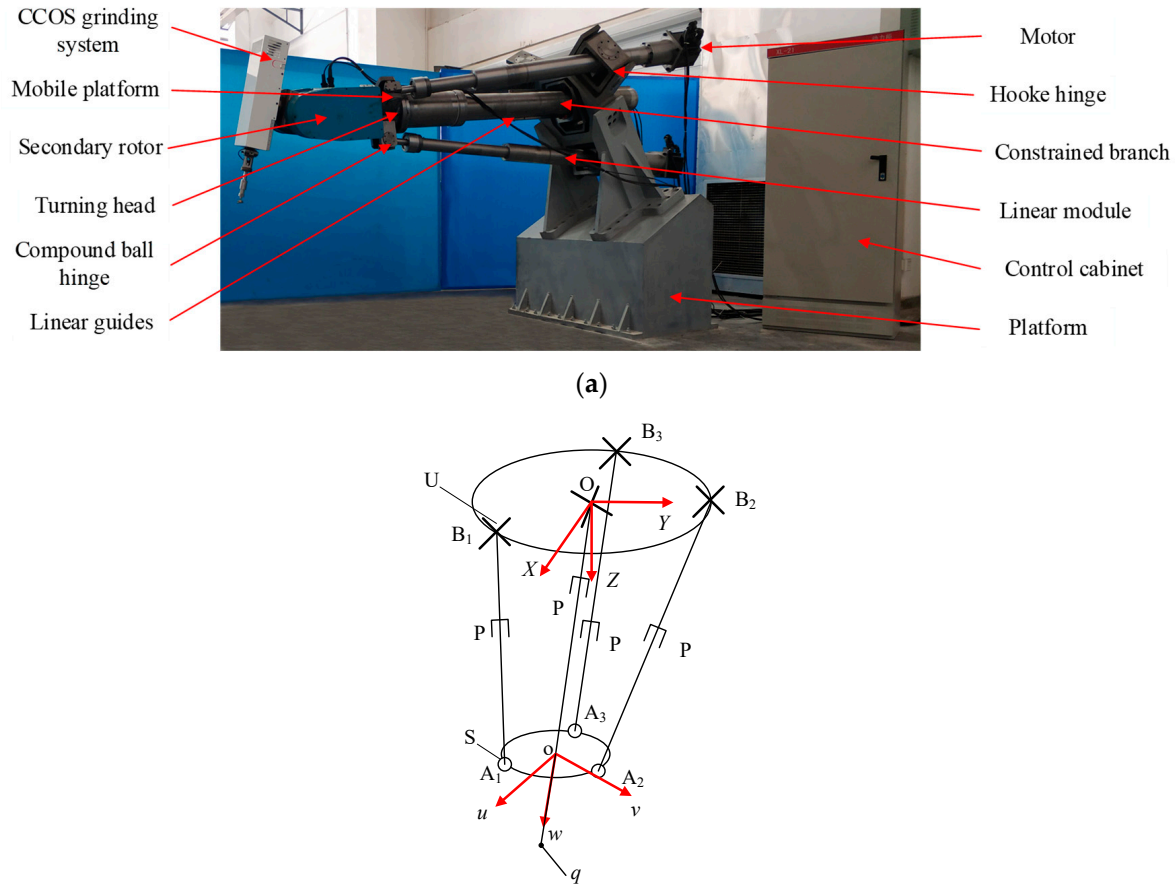


Figure 2. Parallel robot. (**a**) Prototype. (**b**) Parallel partial topology diagram.

The position $\boldsymbol{x}_{ai}$, velocity $\dot{\boldsymbol{x}}_{ai}$, and acceleration $\ddot{\boldsymbol{x}}_{ai}$ of point A in the coordinate system *O*-*XYZ* are given by Equation (3).

$$\begin{cases} \boldsymbol{x}_{ai} = \boldsymbol{P} + \boldsymbol{R} \cdot \boldsymbol{a}_i = \boldsymbol{b}_i + l_i \boldsymbol{e}_i \\ \dot{\boldsymbol{x}}_{ai} = \dot{l}_i \boldsymbol{e}_i + l_i \boldsymbol{\omega}_i \times \boldsymbol{e}_i \\ \ddot{\boldsymbol{x}}_{ai} = \ddot{l}_i \boldsymbol{e}_i + l_i \dot{\boldsymbol{\omega}}_i \times \boldsymbol{e}_i + l_i \boldsymbol{\omega}_i \times (\boldsymbol{\omega}_i \times \boldsymbol{e}_i) + 2\dot{l}_i \boldsymbol{\omega}_i \times \boldsymbol{e}_i \end{cases} \tag{3}$$

The length of the drive branch l_i, the expansion speed $\dot{l}_i$, and the expansion acceleration $\ddot{l}_i$ are given by Equation (4).

$$\begin{cases} l_i = \sqrt{(\boldsymbol{R} \cdot \boldsymbol{a}_i + \boldsymbol{P} - \boldsymbol{b}_i)^2} \\ \dot{l}_i = (\boldsymbol{\omega} \times (\boldsymbol{R} \cdot \boldsymbol{a}_i)) \cdot \boldsymbol{e}_i \\ \ddot{l}_i = \left[\dot{\boldsymbol{\omega}} \times (\boldsymbol{R} \cdot \boldsymbol{a}_i) + \boldsymbol{\omega} \times (\boldsymbol{\omega} \times (\boldsymbol{R} \cdot \boldsymbol{a}_i))\right] \cdot \boldsymbol{e}_i + l_i \boldsymbol{\omega}_i \cdot \boldsymbol{\omega}_i^{\mathrm{T}} \end{cases} \tag{4}$$

The angular velocity $\boldsymbol{\omega}_i$ and the angular acceleration $\dot{\boldsymbol{\omega}}_i$ of the driving branch are given by Equation (5).

$$\begin{cases} \boldsymbol{\omega}_i = \frac{\boldsymbol{e}_i \times (\boldsymbol{\omega} \times (\boldsymbol{R} \cdot \boldsymbol{a}_i))}{l_i} \\ \dot{\boldsymbol{\omega}}_i = \frac{\boldsymbol{e}_i \times \left[\dot{\boldsymbol{\omega}} \times (\boldsymbol{R} \cdot \boldsymbol{a}_i) + \boldsymbol{\omega} \times (\boldsymbol{\omega} \times (\boldsymbol{R} \cdot \boldsymbol{a}_i))\right] - 2 l_i \boldsymbol{\omega}_i}{l_i} \end{cases} \tag{5}$$

The centroid velocity $\boldsymbol{v}_i$ and the centroid acceleration $\boldsymbol{a}_i$ of the driving branch are given by Equation (6).

$$\begin{cases} \boldsymbol{v}_i = \dot{l}_i \boldsymbol{e}_i + \frac{l_i}{2} \boldsymbol{\omega}_i \times \boldsymbol{e}_i \\ \boldsymbol{a}_i = \ddot{l}_i \boldsymbol{e}_i + \frac{l_i}{2} \left[\dot{\boldsymbol{\omega}}_i \times \boldsymbol{e}_i + \boldsymbol{\omega}_i \times (\boldsymbol{\omega}_i \times \boldsymbol{e}_i) \right] \end{cases} \tag{6}$$

The mechanism driving the Jacobian matrix can be further calculated as given by Equation (7).

$$J = \begin{pmatrix} e_1 & \left[\ddot{l}_1 e_1 + \frac{l_1}{2} \left(\dot{\omega}_1 \times e_1 + \omega_1 \times (\omega_1 \times e_1) \right) \right] \times e_1 \\ e_2 & \left[\ddot{l}_2 e_2 + \frac{l_2}{2} \left(\dot{\omega}_2 \times e_2 + \omega_2 \times (\omega_2 \times e_2) \right) \right] \times e_2 \\ e_3 & \left[\ddot{l}_3 e_3 + \frac{l_3}{2} \left(\dot{\omega}_3 \times e_3 + \omega_3 \times (\omega_3 \times e_3) \right) \right] \times e_3 \end{pmatrix} \tag{7}$$

The pose of the driving limb $B_iA_i$with respect to the reference frame *O-XYZ* is given by Equation (8).

$$R_i = \begin{bmatrix} c\beta_i c\gamma_i - s\alpha_i c\beta_i s\gamma_i & -c\alpha_i s\gamma_i & s\beta_i c\gamma_i + s\alpha_i c\beta_i s\gamma_i \\ c\beta_i s\gamma_i + s\alpha_i c\beta_i c\gamma_i & c\alpha_i c\gamma_i & s\beta_i s\gamma_i - s\alpha_i c\beta_i c\gamma_i \\ -c\alpha_i s\beta_i & s\alpha_i & c\alpha_i c\beta_i \end{bmatrix} \tag{8}$$

where α_i and β_i denote the rotation angles about the *X*-axis and *Y*-axis, respectively, $\gamma_i = \frac{\pi}{6} + \frac{2\pi}{3}(i-1), i = 1, 2, 3$.

The orientation angles of the limb B_iA_i are given by Equation (9), and the active branch gesture vector is shown in Figure 3.

$$\begin{cases} \alpha_i = \arcsin\left(w_{ix} \cos\gamma_i + w_{iy} \sin\gamma_i \right) \\ \beta_i = \arctan\left(\frac{w_{ix} \sin\gamma_i - w_{iy} \cos\gamma_i}{w_{iz}} \right) \end{cases} \tag{9}$$

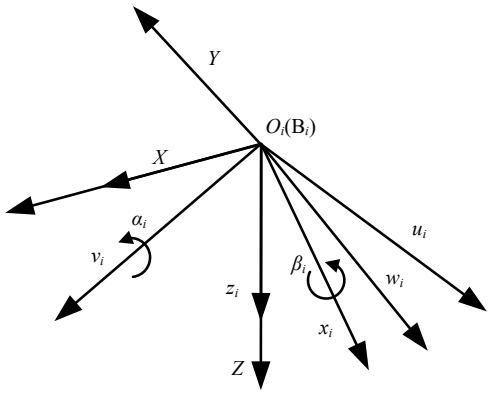


Figure 3. Active branch gesture vector.

3. Institutional Statics Analysis

The static analysis of each mechanism component is carried out by the rod removal method. The static equilibrium equation is established to solve for the joint reaction forces of each component of the parallel mechanism, and the general dynamic model is established by the static analysis results.

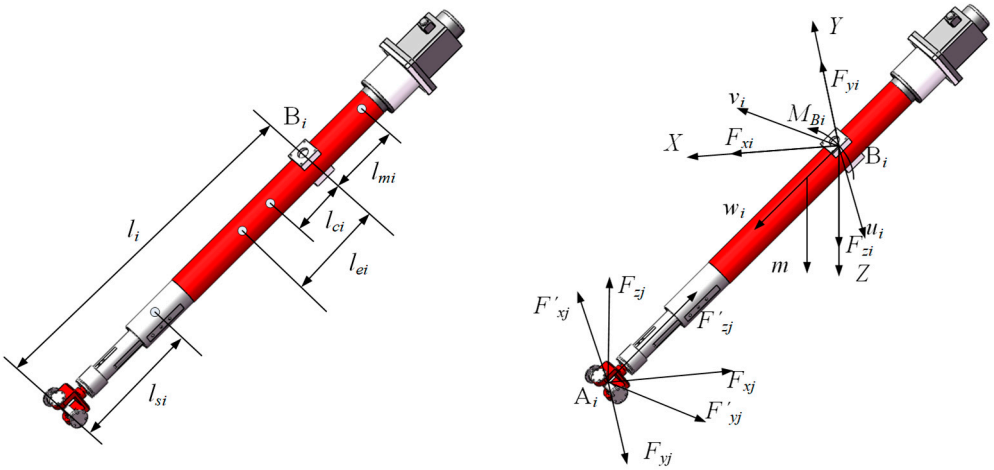
3.1. Static Analysis of the Driving Chain

As shown in Figure 4a, the quality of the drive chain includes three parts: m_1 is the quality of the drive chain located at the back end of the fixed platform; m_2 is the quality

of the drive chain located at the front end of the fixed platform; m_3 is the quality of the telescopic rod. The quality of the whole drive chain is m. So, the position of the center of mass of the driving limb is given by Equation (10).

$$m_2 l_{ei} - m_1 l_{mi} + m_3(l_i - l_{si}) = m l_{ci} \tag{10}$$

where l_{mi} is the distance from the centroid of the driving branch at the rear end of the fixed platform to the fixed hinge point B_i. l_i is the effective length of the drive branch, and l_{ci} is the distance from the centroid of the drive branch to the fixed hinge point B_i. l_{ei} is the distance from the centroid of the driving branch at the front end of the fixed platform to the fixed hinge point B_i, and l_{si} is the distance of the telescopic rod from the moving hinge point A_i.



(**a**) (**b**)

Figure 4. Active branch gesture vector. (**a**) Drive chain centroid analysis. (**b**) Static analysis of driving chain.

So, the centroid position of the drive branch is given by Equation (11).

$$l_{ci} = \frac{m_2 l_{ei} - m_1 l_{mi} + m_3(l_i - l_{si})}{m} \tag{11}$$

The force analysis of the drive branch is shown in Figure 4b. The Hooke hinge that drives the branch has three constrained reaction forces $\boldsymbol{F}_i = \left[F_{xi}, F_{yi}, F_{zi}\right]^{\mathrm{T}}$ (i = 1, 2, 3) and a restraining torque $\boldsymbol{M}_i = [0, 0, M_{Bi}]^{\mathrm{T}}$. The composite ball hinge that drives the chain has three restraining reaction forces $\boldsymbol{F}_j = \left[F_{xj}, F_{yj}, F_{zj}\right]^{\mathrm{T}}$ (j = 4, 5, 6) for the automatic platform. It is assumed that the reaction forces of the spherical pair i are $\boldsymbol{F}'_j = \left[F'_{xj}, F'_{yj}, F'_{zj}\right]^{\mathrm{T}}$, $\boldsymbol{F}'_j = \boldsymbol{R} \cdot \boldsymbol{F}_j$. Then, when the driving branch is in static balance and the fixed hinge point B_i of the driving hinge is taken, the forces balance equation and the torques balance equation are given by Equation (12).

$$\begin{cases} \boldsymbol{F}_i + \boldsymbol{F}_j + m\boldsymbol{G} = 0 \\ \boldsymbol{l}'_i \times \boldsymbol{F}'_j + \boldsymbol{l}'_{ci} \times m\boldsymbol{G} = 0 \end{cases} \tag{12}$$

where $\boldsymbol{G} = [0, 0, g]^{\mathrm{T}}$, drive vector $\boldsymbol{l}_i = \left[l_{xi}, l_{yi}, l_{zi}\right]^{\mathrm{T}}$.

3.2. Static Analysis of Constrained Branched Chain

As shown in Figure 5, the forces condition of the constrained branch in the fixed coordinate system *O-XYZ* is calculated as follows: The constrained branch has a gravity of $m_4 g$ and a constrained branch length of l_4. The Hooke hinge with constrained branches has three

constrained reaction forces $\boldsymbol{F}_4 = \left[F_{4x}, F_{4y}, F_{4z}\right]^{\mathrm{T}}$ and a constrained torque $\boldsymbol{M}_4 = [0, 0, M_{4z}]^{\mathrm{T}}$ from the fixed platform. There are three restraining forces $\boldsymbol{F}_4' = \left[F_{4x}', F_{4y}', F_{4z}'\right]^{\mathrm{T}}$ and three restraining torques $\boldsymbol{M}_4' = \left[M_{4x}', M_{4y}', M_{4z}'\right]^{\mathrm{T}}$ at the junction between the constrained chain and the fixed platform. When the constrained chain is in static equilibrium and the O is taken from the center of the platform, the forces balance equation and the torques balance equation are given by Equation (13).

$$\begin{cases} \boldsymbol{F}_4 + \boldsymbol{F}_4' + m_4\boldsymbol{G} = 0 \\ \boldsymbol{M}_4' + \boldsymbol{M}_4 + \boldsymbol{l}_4 \times \boldsymbol{F}_4' = 0 \end{cases} \tag{13}$$

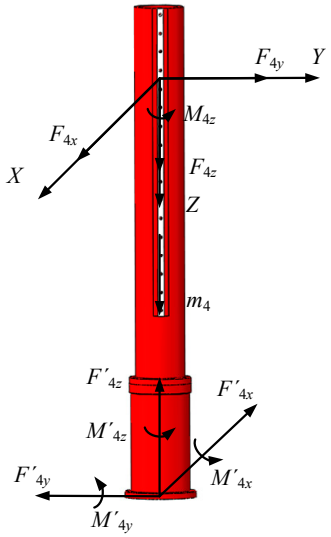


Figure 5. Stress diagram of constrained branched chain.

3.3. Static Analysis of the Dynamic Platform

As shown in Figure 6, the forces of the moving platform in the fixed coordinate system *O-XYZ* are calculated as follows: The moving platform has a gravity of $m_5 g$, and the hinge restraint reaction of the moving platform is $\boldsymbol{F}_j = \left[F_{xj}, F_{yj}, F_{zj}\right]^{\mathrm{T}}$. There are three constrained reaction forces $\boldsymbol{F}_4' = \left[F_{4x}', F_{4y}', F_{4z}'\right]^{\mathrm{T}}$ and three constraint torques $\boldsymbol{M}_4' = \left[M_{4x}', M_{4y}', M_{4z}'\right]^{\mathrm{T}}$ from the constrained branch. When the forces platform is analyzed, the mass of the front end of the robot and the torques of inertia are simplified to external loads. The actual load on the moving platform is related to the actual motion trajectory of the mechanism, which is often a compound generalized force $\boldsymbol{F}_w$. This includes three external binding forces $\boldsymbol{F}' = \left[F_x, F_y, F_z\right]^{\mathrm{T}}$ and three constraining torques $\boldsymbol{M}' = \left[M_x, M_y, M_z\right]^{\mathrm{T}}$. The forces balance equation when the moving platform is in static equilibrium and the torques balance equations of the upper platform to the centroid o point are given by Equation (14).

$$\begin{cases} \boldsymbol{F}' + \boldsymbol{F}_4' + m_5\boldsymbol{G} + \sum\limits_{j=4}^{6} \boldsymbol{F}_j = 0 \\ \boldsymbol{M}' + \boldsymbol{M}_4' + \sum\limits_{j=4}^{6} b \cdot \boldsymbol{F}_j = 0 \end{cases} \tag{14}$$

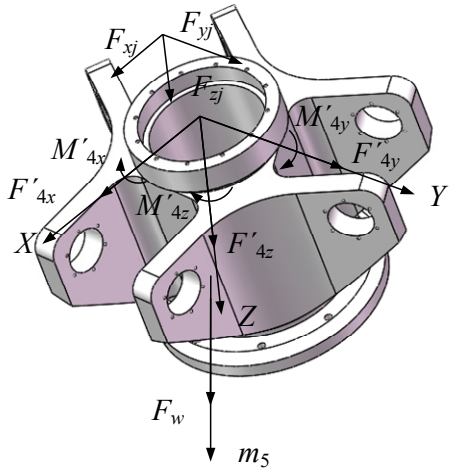


Figure 6. Stress diagram of dynamic platform.

Combining Equations (12)–(14) together can form a 5 × 6-dimensional scalar system of equations (six forces balance equations can be listed from each active member). Each drive branch contains 6 unknown forces/torques, and the constrained branch contains 12 unknown forces/torques. There are 30 unknown forces/torques.

The matrix of the system of equations is given by Equation (15).

$$\boldsymbol{AX} = \boldsymbol{B} \tag{15}$$

where $\boldsymbol{A}$ is the parameter matrix; $\boldsymbol{B}$ is the known load matrix; $\boldsymbol{X}$ represents the constraint reaction forces. That is, the unknown quantity of the equation is $\boldsymbol{X} = \boldsymbol{A}^{-1}\boldsymbol{B}$.

After determining the total binding forces/torques for each construction of the mechanism, the driving forces $\boldsymbol{\tau}_i$ are given by Equation (16).

$$\boldsymbol{\tau}_i = \boldsymbol{S}_i \cdot \boldsymbol{F}_j + m\boldsymbol{S}_i \cdot \boldsymbol{G} \tag{16}$$

where m and $\boldsymbol{S}_i$ are the mass and the unit vector of the drive rod.

4. "Coulomb + Viscous" Friction Model

The mathematical expression of the Coulomb + Viscous model is given by Equation (17).

$$f(v) = f_v v + f_c \mathrm{sgn}(v) \tag{17}$$

where v is the relative sliding speed, f_v is the viscous friction coefficient, f_c is the coulomb friction, and $\mathrm{sgn}(v)$ is the sign function.

The friction torques introduced by the rotating pair are shown in Figure 7, where r_f is the radius of the rotating pair, ω is the angular velocity, and $\boldsymbol{M}_f$ is the friction torques, $\boldsymbol{F}_n$ is the normal force at the revolute joint, $\boldsymbol{F}_t$ is the tangential force, and $\boldsymbol{F}_r$ is the resultant force of the normal and tangential forces, which is always tangent to the friction circle.

(1) The frictional torque in the Hooke's joint is given by Equation (18).

$$\begin{cases} M^u_{fx} = [\mu_v \omega^u_x + \mu_c |\boldsymbol{F}^u| \mathrm{sgn}(\omega^u_x)] \cdot R_u \\ M^u_{fy} = \left[\mu_v \omega^u_y + \mu_c |\boldsymbol{F}^u| \mathrm{sgn}\left(\omega^u_y\right)\right] \cdot R_u \end{cases} \tag{18}$$

where $\boldsymbol{F}^u$ are the joint reaction forces of the Hooke hinge, μ_v is the viscous friction coefficient, μ_c is the coulomb friction coefficient, R_u is the friction radius, ω^u_x and ω^u_y are the rotation speeds around the X-axis and Y-axis, respectively.

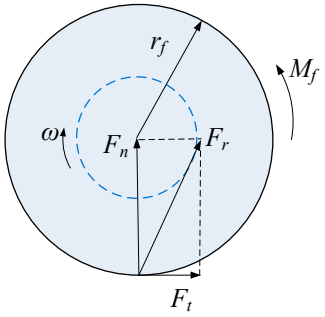


Figure 7. Schematic diagram of the rotating secondary friction torques.

(2) The frictional torque in the ball hinge is given by Equation (19).

$$\begin{cases} M^s_{fx} = [\mu_v \omega^s_x + \mu_c |\boldsymbol{F}^s| \mathrm{sgn}(\omega^s_x)] \cdot R_s \\ M^s_{fy} = \left[\mu_v \omega^s_y + \mu_c |\boldsymbol{F}^s| \mathrm{sgn}\left(\omega^s_y\right)\right] \cdot R_s \\ M^s_{fz} = [\mu_v \omega^s_z + \mu_c |\boldsymbol{F}^s| \mathrm{sgn}(\omega^s_z)] \cdot R_s \end{cases} \tag{19}$$

where $\boldsymbol{F}^s$ are the joint reaction forces of the composite ball hinge, R_s is the friction circle radius, and ω^s_x, ω^s_y, and ω^s_z are the rotation speeds around the X-axis, Y-axis, and Z-axis, respectively.

(3) The frictional torque and friction forces in the ball screw are given by Equation (20).

$$\begin{cases} M^c_{fz} = [\mu_v \omega^c_z + \mu_c |\boldsymbol{F}^c| \mathrm{sgn}(\omega^c_z)] \cdot R_c \\ f^c_{fz} = \mu_v \dot{z}^c + \mu_c |\boldsymbol{F}^c| \mathrm{sgn}\left(\dot{z}^c\right) \end{cases} \tag{20}$$

where $\boldsymbol{F}^c$ are the joint reaction forces of the linear module, R_c is the friction circle radius, ω^c_z is the rotation speed around Z-axis, and $\dot{z}^c$ is the movement speed.

(4) The frictional forces in the linear guide are given by Equation (21).

$$f^l_{fz} = \mu_v \dot{z}^l + \mu_c \left|\boldsymbol{F}^l\right| \mathrm{sgn}\left(\dot{z}^l\right) \tag{21}$$

where $\boldsymbol{F}^l$ are the joint reaction forces of the linear guide, and $\dot{z}^l$ is the speed.

5. Dynamic Simulation Analysis

5.1. Dynamic Analysis of Driving Chain

The inertial forces that the driving branch receives during movement come from two aspects: the inertial forces generated by the rotation of the driving branch in the space and the inertial forces caused by the self-driving. As shown in Figure 8, the Hooke joint introduces two friction moments, denoted as $\boldsymbol{M}^u_i = \left[M^u_{fix}, M^u_{fiy}, 0\right]^{\mathrm{T}}$; a frictional force $\boldsymbol{F}^p_i = \left[0, 0, F^p_{fiz}\right]^{\mathrm{T}}$ and a frictional torque $\boldsymbol{M}^p_i = \left[0, 0, M^p_{fiz}\right]^{\mathrm{T}}$ are introduced into the screw. Three frictional torques $\boldsymbol{M}^s_j = \left[M^s_{fjx}, M^s_{fjy}, M^s_{fjz}\right]^{\mathrm{T}}$ are introduced into the composite ball hinge. The dynamic equilibrium equation of the driving branch is given by Equation (22).

$$\begin{cases} \boldsymbol{F}_i + \boldsymbol{F}_j + m(\ddot{x}_{ai} + \ddot{\boldsymbol{l}}_i + \boldsymbol{G}) + \boldsymbol{F}^p_{fiz} = 0 \\ \boldsymbol{J}'_i \dot{\boldsymbol{\omega}}_{Bi} + \boldsymbol{\omega}_{Bi} \times \boldsymbol{J}'_i \boldsymbol{\omega}_{Bi} + \boldsymbol{l}_i \times \boldsymbol{F}_j + \boldsymbol{l}_{ci} \times m\boldsymbol{G} + \boldsymbol{M}^u_i + \boldsymbol{M}^p_i + \boldsymbol{M}^s_j = 0 \end{cases} \tag{22}$$

where $\boldsymbol{J}'_i = \boldsymbol{R}_i \cdot \boldsymbol{J}_i \cdot \boldsymbol{R}^{\mathrm{T}}_i$, $\boldsymbol{J}_i$ are the torques of inertia, $\boldsymbol{J}_{ix} = \boldsymbol{J}_{iy} = \boldsymbol{J}_{iz} = \frac{1}{3} m l^2_i$, m is the quality of the drive branch, $\boldsymbol{l}_i = \left[l_{ix}, l_{iy}, l_{iz}\right]^{\mathrm{T}}$, $\boldsymbol{l}_{ci} = \left[l_{cix}, l_{ciy}, l_{ciz}\right]^{\mathrm{T}}$, $\boldsymbol{F}_i = \left[F_{ix}, F_{iy}, F_{iz}\right]^{\mathrm{T}}$, $\boldsymbol{F}_j = \left[F_{jx}, F_{jy}, F_{jz}\right]^{\mathrm{T}}$.

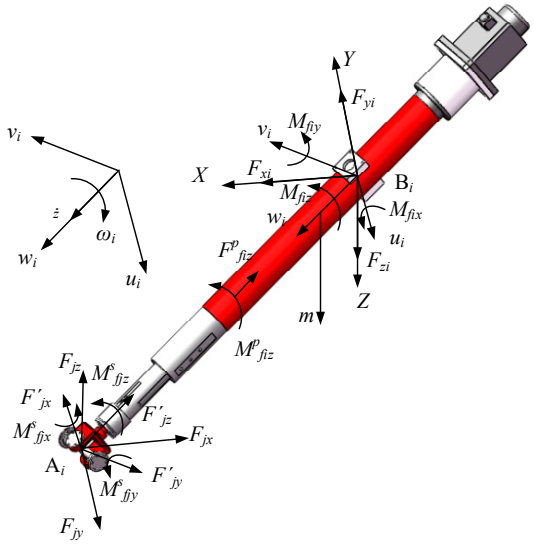


Figure 8. Stress diagram of driving chain.

5.2. Dynamic Analysis of Constrained Branching

The dynamic analysis of constrained branching chains is shown in Figure 9. Among them, the Hooke hinge introduces two friction torques $\boldsymbol{M}^u = \left[M^u_{f4x}, M^u_{f4y}, 0\right]^{\mathrm{T}}$, the linear guide rail introduces a friction force $\boldsymbol{F}^l = \left[0, 0, F^l_{f4z}\right]^{\mathrm{T}}$ and a friction torque $\boldsymbol{M}^l = \left[0, 0, M^l_{f4y}\right]^{\mathrm{T}}$, of which $M^l_{f4y} = F^l_{f4z} r_4$. r_4 is to restrict the radius of the branch chain. The dynamic equations of the constrained follower chain are given by Equation (23).

$$\begin{cases} \boldsymbol{F}_4 + \boldsymbol{F}'_4 + m_4(\ddot{\boldsymbol{z}} + \boldsymbol{G}) + \boldsymbol{F}^l = 0 \\ \boldsymbol{M}_4 + \boldsymbol{M}'_4 + \boldsymbol{l}_4 \times \boldsymbol{F}'_4 + \boldsymbol{J}'_4 \dot{\omega}_4 + \omega_4 \times \boldsymbol{J}'_4 \omega_4 + \boldsymbol{M}^u + \boldsymbol{M}^l = 0 \end{cases} \tag{23}$$

where $\boldsymbol{J}'_4 = \boldsymbol{R} \cdot \boldsymbol{J}_4 \cdot \boldsymbol{R}^{\mathrm{T}}$, $\boldsymbol{J}_4$ are the torques of inertia of the constrained branch chain, $\boldsymbol{J}_{4x} = \boldsymbol{J}_{4y} = \boldsymbol{J}_{4z} = \frac{1}{3} m_4 l_4^2$, $\ddot{z}$ is the acceleration of the center of mass of the moving platform, and ω_4 is the rotational speed of the restrained chain.

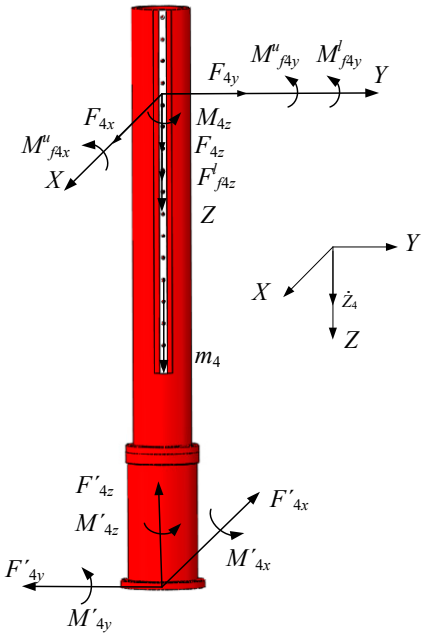


Figure 9. Dynamic analysis of constrained branched chain.

5.3. Dynamic Analysis of Fixed Platform

The dynamic analysis of the moving platform is shown in Figure 10. The dynamic equilibrium equation of the moving platform is given by Equation (24).

$$\begin{cases} \boldsymbol{F} + \boldsymbol{F}_4' + m_5(\boldsymbol{G} + \ddot{\boldsymbol{z}}) + \sum_{j=4}^{6} \boldsymbol{F}_j = 0 \\ \boldsymbol{M} + \boldsymbol{M}_4' + \sum_{j=4}^{6} b \cdot \boldsymbol{F}_j + \boldsymbol{J}_5' \dot{\omega}_5 + \omega_5 \times \boldsymbol{J}_5' \omega_5 + \boldsymbol{M}_j'^{s} = 0 \end{cases} \tag{24}$$

where $\boldsymbol{F}_w = [\boldsymbol{F}, \boldsymbol{M}]$, $\boldsymbol{F} = \left[F_x, F_y, F_z\right]^{\mathrm{T}}$ are the external forces received by the moving platform. $\boldsymbol{M} = [M_x, M_y, M_z]^T$ are the external torques received by the moving platform; $\boldsymbol{J}_5' = \boldsymbol{R} \cdot \boldsymbol{J}_5 \cdot \boldsymbol{R}^{\mathrm{T}}$. $\boldsymbol{J}_5$ are the torques of inertia of the coordinate system *o-uvw*, $\boldsymbol{J}_{5x} = \boldsymbol{J}_{5y} = \boldsymbol{J}_{5z} = \frac{1}{3} m_5 r^2$. r is the radius of the moving platform. ω_5 is the rotation speed of the fixed platform.

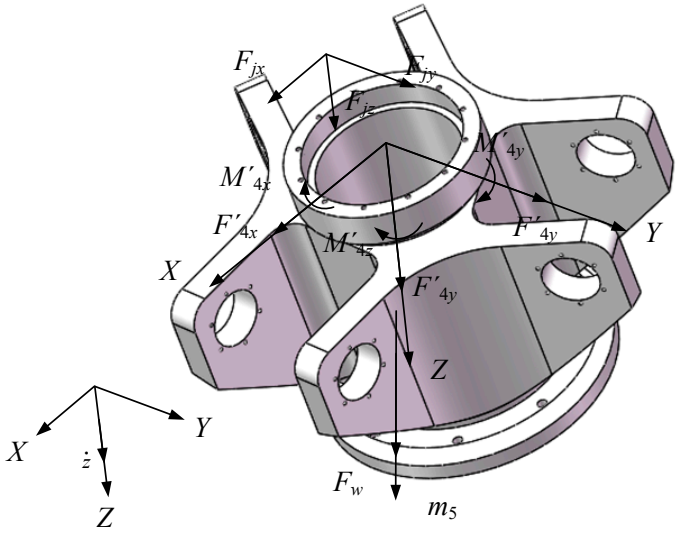


Figure 10. Stress diagram of fixed platform.

The dynamic equation accounting for joint friction can be expressed as Equation (25).

$$\boldsymbol{A}\boldsymbol{X} = \boldsymbol{B} + \boldsymbol{Q}^f \tag{25}$$

where $\boldsymbol{A}$, $\boldsymbol{B}$, and $\boldsymbol{X}$ have the same mathematical meaning as $\boldsymbol{A}$, $\boldsymbol{B}$, and $\boldsymbol{X}$ in Equation (15), and $\boldsymbol{Q}^f$ is a moving motion secondary friction vector introduced in the parallel mechanism based on the "Coulomb + Viscous" friction model.

Considering the friction between the driving branch and the restraining branch, the driving forces $\boldsymbol{\tau} = [\tau_1, \tau_2, \tau_3]^{\mathrm{T}}$ of the parallel mechanism are given by Equation (26).

$$\tau_i = \boldsymbol{F}_i \cdot \boldsymbol{S}_i + m\boldsymbol{S}_i \cdot \boldsymbol{G} + m\left[\dot{x}_{ai} + \ddot{\boldsymbol{l}}_i\right]^{\mathrm{T}} \cdot \boldsymbol{S}_i + f_i \tag{26}$$

where f_i is the secondary motion pair friction.

The process of solving the dynamics is shown in Figure 11. First, the constrained reaction forces $\boldsymbol{X}_1$ are obtained according to the static equations of Equation (15). Secondly, the motion secondary friction vector $\boldsymbol{Q}^f$ is calculated according to the obtained constraint reaction forces. Then, according to the dynamic constraint equation of Equation (25), the joint reaction forces $\boldsymbol{F}^1$ considering the secondary friction of the shutdown motion are obtained. Further, the parallel mechanism driving forces $\boldsymbol{\tau}^1$ are obtained according to the

driving calculation equation. Finally, the above process is repeated until the desired driving forces converge to obtain $\boldsymbol{X}_n$, $\boldsymbol{F}^n$, $\boldsymbol{\tau}^n$, and $\boldsymbol{Q}_n^f$, among them (n = 1, 2, 3. . .).

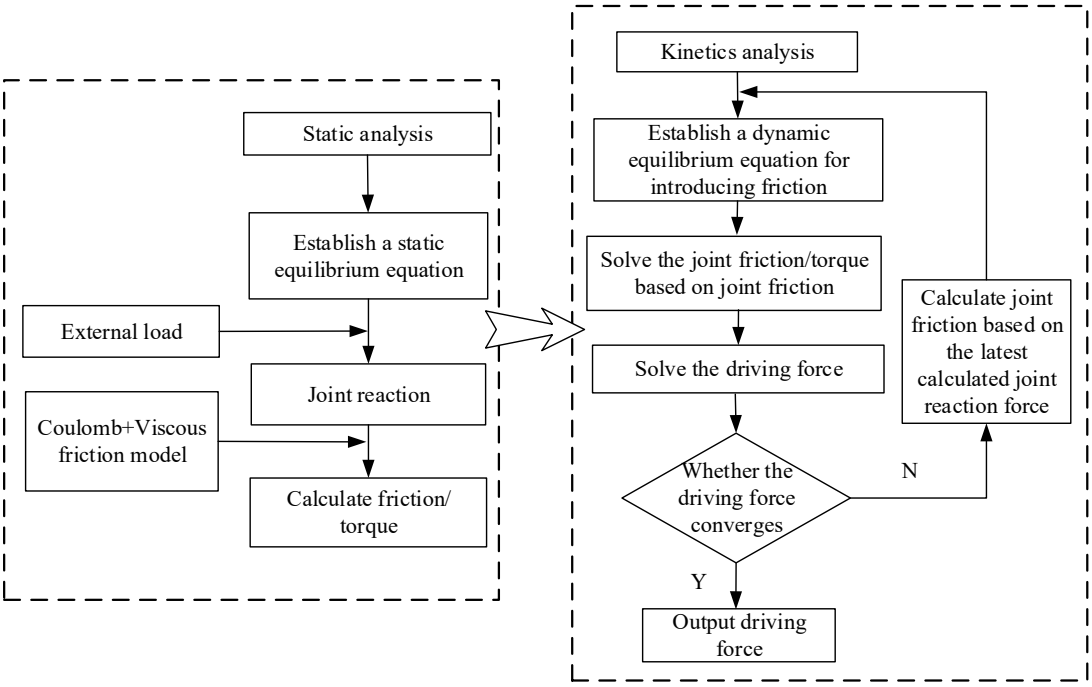


Figure 11. Dynamics solution process.

5.4. Dynamics Simulation Analysis of Robot

At present, the surface shapes of large optical mirrors are mostly irregular curved surfaces, which makes the movement trajectory and stress state of the robot more complex during processing and is not convenient for verifying the accuracy of the established model. The robot here is given a circular trajectory curve, and the parameter equation is given by Equation (27).

$$\begin{cases} x = 400\cos 2\pi t \\ y = 400\sin 2\pi t \quad t = [0{:}1] \\ z = 1200 - 0 \times t \end{cases} \tag{27}$$

The parameters of the robot components are listed in Table 1.

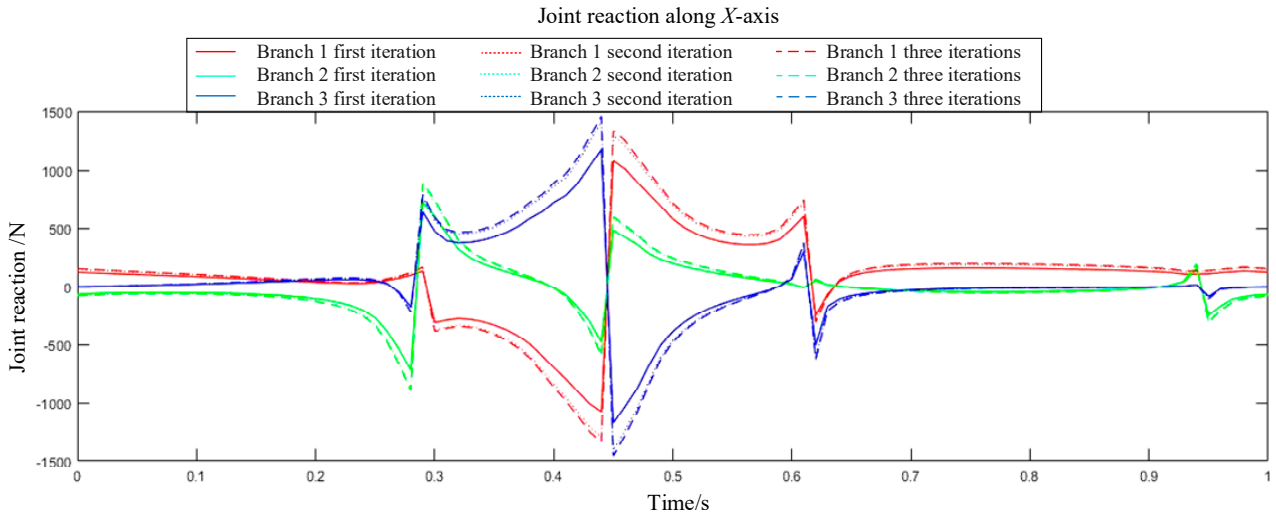
Table 1. Parameter values of each component of the parallel mechanism.

Parameter	Numerical Value	Parameter	Numerical Value
Fixed platform circumscribing radius/mm	450	Platform quality/kg	151.78
Moving platform circumscribing radius/mm	150	Composite ball hinge quality/kg	5.4
Active branch total mass/kg	86	Constrained branch radius/mm	50
Fixed platform back-end drive branch quality/kg	25.8	Hooke hinge bearing rotation radius/mm	32.525
Platform front end drive branch quality/kg	35.6	Composite ball hinge bearing rotation radius/mm	13
Telescopic rod quality/kg	25.6	Gravity acceleration/(m/s^2)	9.8
Constrained branch quality/kg	112.25	Coulomb friction coefficient	0.12
Dynamic platform quality/kg	32.41	Adhesive friction coefficient/(N·S/m)	0.02

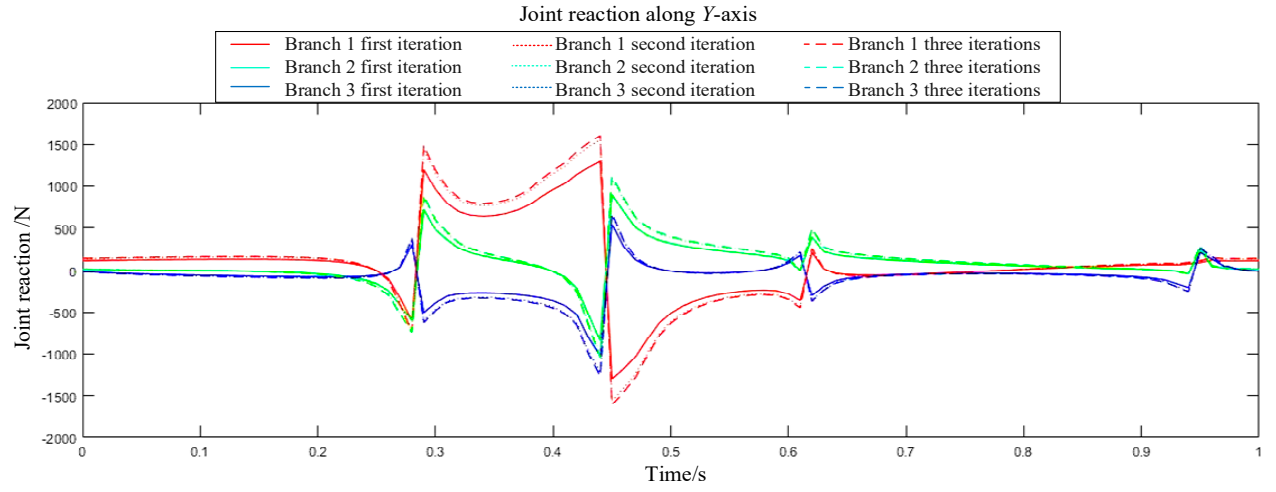
Here this paper assumes that the external load on the moving platform is $\boldsymbol{F} = [200\ \text{N}, 200\ \text{N}, 200\ \text{N}]$, $\boldsymbol{M} = [50\ \text{N.m}, 50\ \text{N.m}, 50\ \text{N.m}]$. According to the above parameters, combined with the analysis results of kinematics and statics, numerical analyses of the established parallel mechanism dynamics model were performed in MATLAB (R2022b)/Simulink. The magnitude of motion pair friction is related to the joint reaction forces, while the motion pair friction in turn affects the magnitude of the joint reaction forces. The iterative process is shown in Figure 11, until the joint reaction forces/torques and the driving forces of the drive branch converge. In the numerical analysis, it was found that the convergence condition was reached in the third iteration, so further iteration was terminated. The result of the third iteration was used as the output force of the driving branch during the movement of the robot.

Figures 12 and 13 display the joint reaction forces/moments in the driving limbs and constraining limbs, respectively. A notable common characteristic is that at time instances t = 0.28 s, 0.45 s, 0.62 s, and 0.95 s, all forces/moments undergo abrupt changes, which are closely related to the predefined helical trajectory. At these specific moments, the resultant motion direction of the moving platform changes abruptly, causing a reversal in the acceleration direction of the driving limbs and thereby imposing impact loads on the mechanism. By comparing the curves from the friction-neglected (first iteration) and friction-considered (third iteration) models, it is observed that after accounting for friction, the maximum joint reaction force in the driving limbs increases by approximately 350 N (Figure 12), while the constraining limbs exhibit a maximum force increase of about 560 N and a moment increase of around 108 N·m (Figure 13). This comparison clearly demonstrates that neglecting friction in conventional dynamic models leads to a significant underestimation of the actual loads on the joint, which is detrimental for fatigue life prediction and reliability assessment of critical robot components.

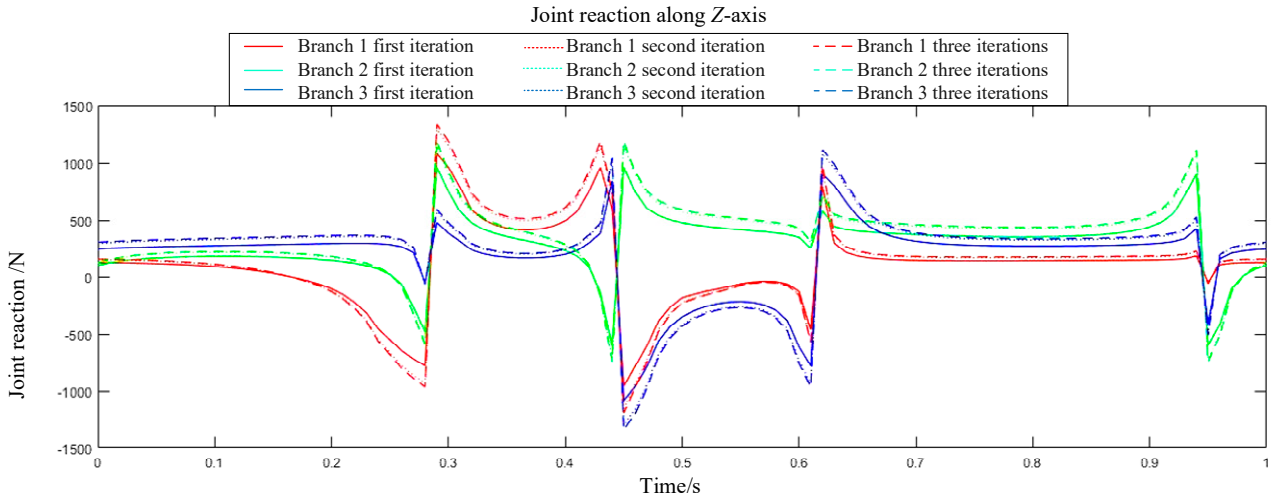
From the analysis results of the driving force in the driving limbs shown in Figure 14, it can be observed that in the friction-included model, the transients in the driving force are sharper. This phenomenon occurs because the "Coulomb + Viscous" friction model incorporates a sign function, sgn(v), at zero-crossing instants of velocity (i.e., the moment of direction reversal), leading to a step change in the friction force and intensifying the dynamic shock in the system. Furthermore, the driving force serves as the direct basis for the design of the robot's servo system. The friction-neglected model (first iteration) predicts a smooth driving force profile with lower amplitude, representing an idealized and overly optimistic prediction that fails to reflect the actual control requirements. In contrast, the friction-considered models (second and third iterations) reveal high-frequency, large-magnitude peaks in the driving force at motion reversal points. This finding carries significant engineering implications: it indicates that the robot's controller and actuators must possess sufficient bandwidth and output headroom to handle these instantaneous peaks; otherwise, trajectory tracking performance may be compromised.



(**a**)



(**b**)



(**c**)

Figure 12. Driving branch joint reaction. (**a**) Joint reaction along *X*-axis. (**b**) Joint reaction along *Y*-axis. (**c**) Joint reaction along *Z*-axis.

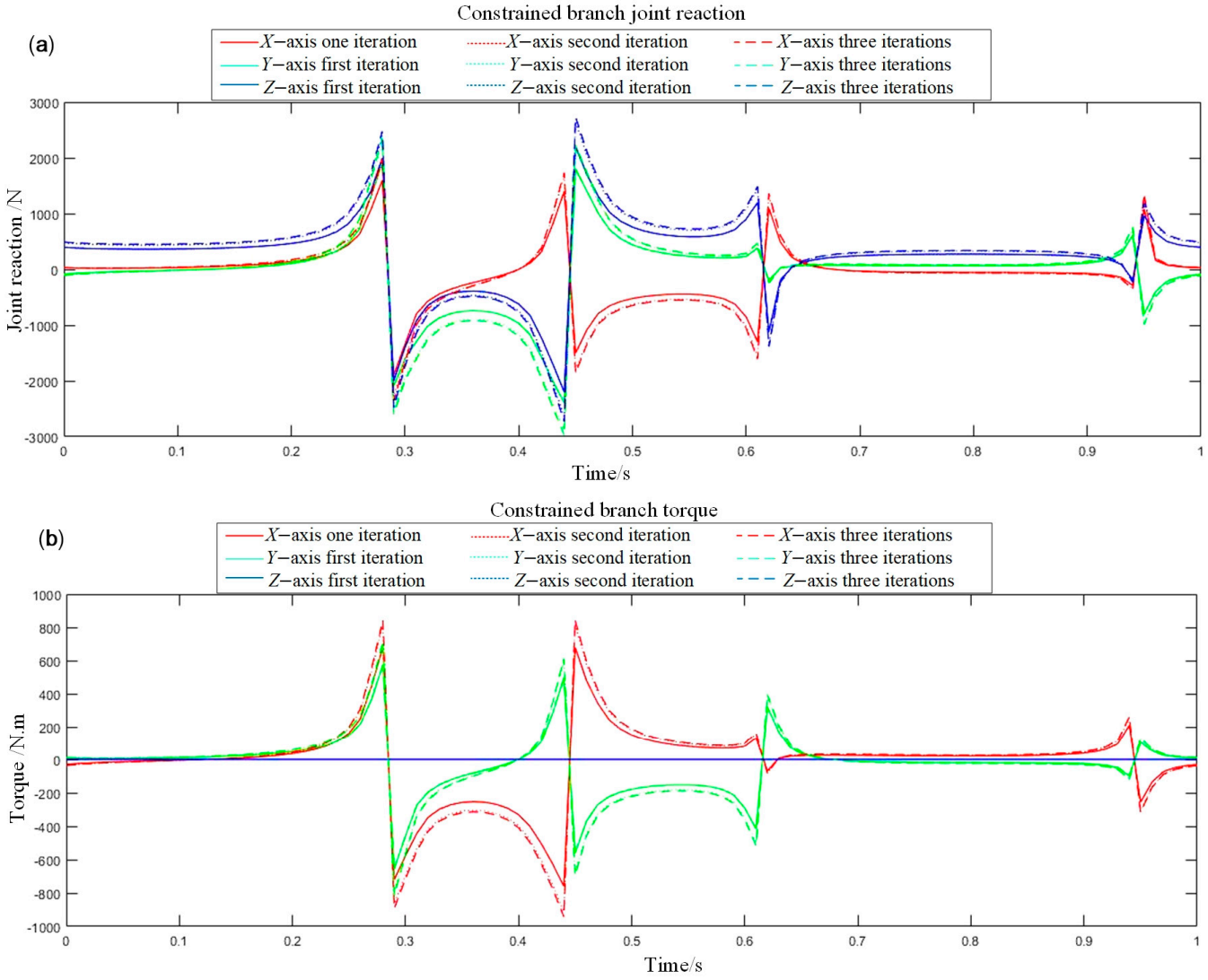


Figure 13. Constrained branch restraint reaction forces/torques. (**a**) Constrained branch joint reaction. (**b**) Constrained branch torques.

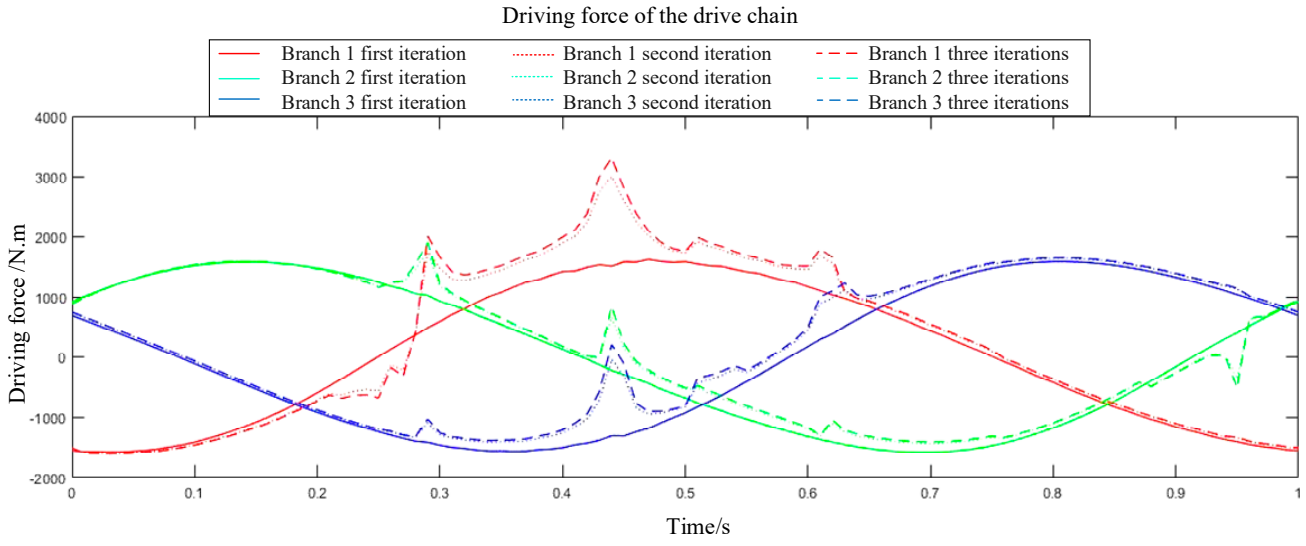


Figure 14. Driving forces of the drive chain.

6. Joint Friction Compensation Based on Feedforward PD Control

When the parallel mechanism completes the task of space transportation, there will be frictions between the various kinematic pairs of the parallel mechanism. Since the working process of the LOMP robot is determined during the working process, the corresponding processing trajectory is also determined correspondingly. So, the motion state of the robot becomes known.

The friction torques model is given by Equation (28).

$$M_f = \begin{bmatrix} M_{fx} \\ M_{fy} \\ M_{fz} \end{bmatrix} = \begin{bmatrix} M^u_{fix} + F^p_{fiz} \cdot (s\beta_i c\gamma_i + s\alpha_i c\beta_i s\gamma_i) + M^s_{fix} + M^u_{f4x} \\ M^u_{fiy} + F^p_{fiz} \cdot (s\beta_i s\gamma_i - s\alpha_i c\beta_i c\gamma_i) + M^s_{fiy} + M^u_{f4y} \\ M^p_{fiz} + M^s_{fiz} \end{bmatrix}, i = 1,2,3 \quad (28)$$

The feedforward PD control is given by Equation (29).

$$\tau = M(q_d)\ddot{q}_d + C(q_d, \dot{q}_d) \cdot \dot{q}_d + g(q_d) + k_p \cdot \Delta q + k_v \cdot \Delta \dot{q} \quad (29)$$

Among them, $M(q)$ is the inertia matrix. $C(q, \dot{q})$ are the centrifugal forces and coriolis forces. $g(q)$ is the gravity term. $\Delta q = q_d - q$, $\Delta \dot{q} = \dot{q}_d - \dot{q}$, K_p, and K_v are the positive definite symmetry matrix parameters.

A block diagram of the robot control system using feedforward PD control is shown in Figure 15.

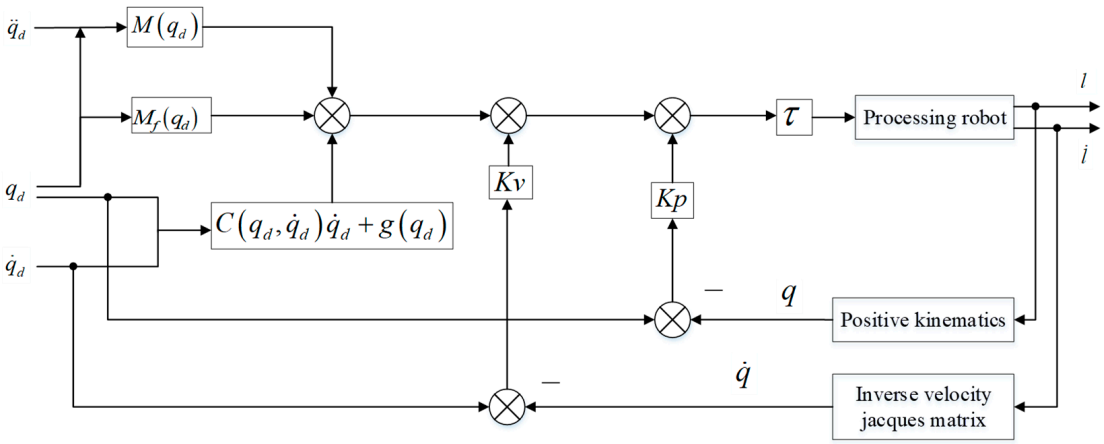


Figure 15. Robot control system based on feedforward PD control.

The closed-loop equation is given by Equation (30).

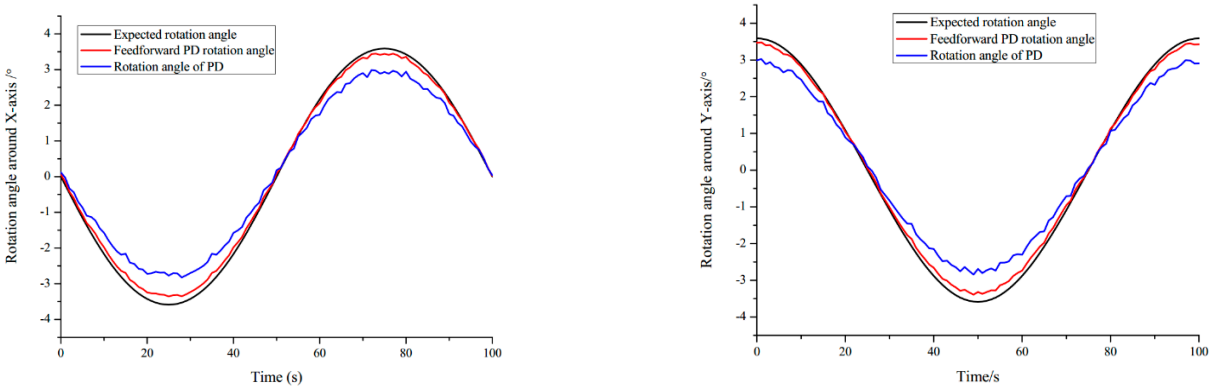
$$\begin{aligned} &M(q)\ddot{q} + C(q, \dot{q}) \cdot \dot{q} + g(q) = \\ &M(q_d)\ddot{q}_d + C(q_d, \dot{q}_d) \cdot \dot{q}_d + g(q_d) + k_p \cdot \Delta q + k_v \cdot \Delta \dot{q} + M_f(q_d) \end{aligned} \quad (30)$$

The optimal PD control parameters for the robot, obtained through simulation analysis in MATLAB (R2022b)/Simulink, are given by Equation (31).

$$\begin{cases} K_p = [diag(46000, 72500, 63500)] \\ K_v = [diag(3850, 4550, 3070)] \end{cases} \quad (31)$$

The simulation results are shown in Figure 16. The results demonstrate that the feedforward PD control enables the robot's trajectory to more closely align with the desired trajectory. In order to verify the reliability of parameters, the "Coulomb + Viscous" friction compensation speed control experiment with the LOMP robot was conducted based on

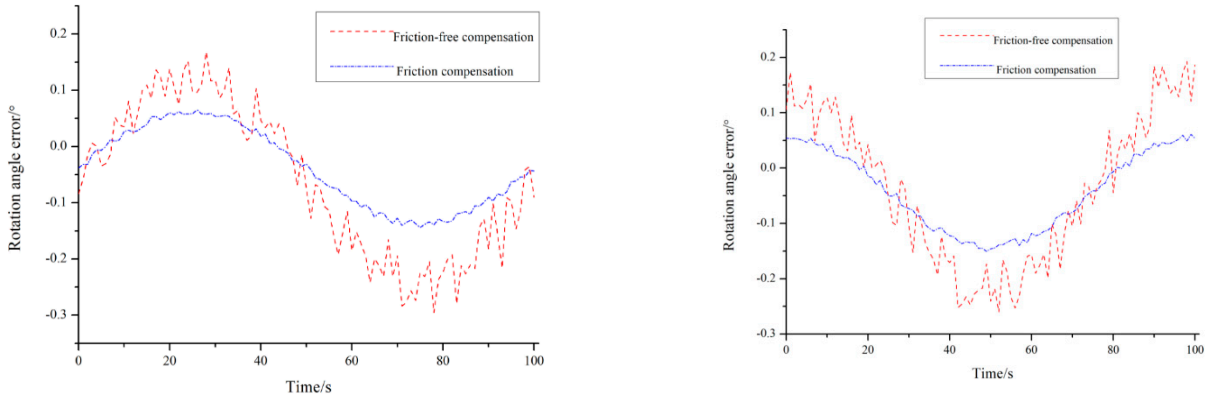
the current loop. In this control system, the motion control card employed was the IMAC motion controller from Delta Tau, which is based on a DSP kernel and communicates with the host computer via an Ethernet port. Both the control and compensation algorithms were developed using the Pewin32 Pro2 software environment, executed on the host computer. This setup facilitates the issuance of control commands to the controller and the retrieval of collected control and feedback data from it. The desired motion trajectory of the processing robot is shown in Equation (27).



(**a**) (**b**)

Figure 16. Dynamic platform rotation angle change. (**a**) Rotation angle change around the X axis. (**b**) Rotation angle change around the Y axis.

As shown in Figure 17, the measured rotational angle error of the driving branch output torque demonstrates that without friction compensation, the moving platform's rotational angle significantly deviates from the theoretical value. After applying compensation based on the established "Coulomb + Viscous" friction model, the tracking errors around the *X*- and *Y*-axis were reduced from 0.295° and 0.286° to 0.134° and 0.128°, respectively. These results confirm that the designed compensator can effectively mitigate the real-time friction effects during mechanism motion.



(**a**) (**b**)

Figure 17. Dynamic platform angle error. (**a**) Angle error around the *X* axis. (**b**) Angle error around the *Y* axis.

7. Discussion

This section aims to provide an in-depth analysis of key simulation and experimental results to elucidate their underlying physical mechanisms and engineering implications.

(1) The simulation results clearly demonstrate the substantial impact of joint friction on the system's dynamic loads. When friction is considered, both the joint reaction forces and

driving forces exhibit sharp peaks at motion reversal instants, with a maximum observed increase of 350 N. This phenomenon originates from the nonlinear step-change characteristic of the friction model at velocity zero-crossings. The resulting dynamic shock loads are significantly higher than those predicted by friction-neglected models. This finding underscores that traditional design methods based on idealized models systematically underestimate the actual loads on critical components, thereby imposing stricter requirements on structural reliability design and actuator selection for the robot.

(2) The feedforward PD compensator, designed based on the aforementioned high-precision model, successfully reduced the moving platform's rotational tracking error by approximately 55%. This validates the effectiveness of the technical pathway: "solving joint reactions via static analysis—accurate friction calculation—feedforward compensation". The principal advantage of this method lies in its feedforward nature, which enables the proactive cancellation of dominant disturbances and thus avoids the inherent latency issues associated with purely feedback-based control.

(3) However, the residual errors persisting after compensation also delineate the boundaries of the present model. These errors may stem from unmodeled dynamic coupling, component flexibility, or more complex friction behaviors (such as the Stribeck effect). This observation precisely indicates that the proposed framework—integrating the "Coulomb + Viscous" model with static analysis—successfully captures the primary factors governing system accuracy. Furthermore, it establishes a reliable research foundation for subsequent integration of more sophisticated models (e.g., flexible-body dynamics, adaptive control) in the pursuit of ultimate precision.

8. Conclusions

This study focuses on enhancing the accuracy of processing large optical mirrors by establishing a high-precision dynamic model that accounts for joint friction in a hybrid robot used for LOMP. And, a feedforward compensation control strategy based on this dynamic model is also designed. Compared to conventional dynamic models that neglect friction, the "Coulomb + Viscous" friction model developed in this work more accurately simulates dynamic loads at critical points such as motion direction reversals, revealing significant abrupt changes in joint reaction forces and driving forces under such conditions. Experimental results demonstrate that the friction compensator, designed based on the proposed model, effectively reduces force output errors caused by joint friction, thereby laying a solid foundation for directly improving the robot's end-effector trajectory accuracy and repeatability.

This research provides a dynamics-based solution for improving the quality of LOMP. By actively compensating for internal frictional disturbances, the uncertainty in the machining process is reduced. This approach decreases the number of traditional "polishing–inspection–polishing" cycles required during LOMP, saving time associated with fixture positioning for inspection and re-positioning for polishing. The study establishes a reliable research foundation for achieving high-precision, efficient processing of large optical mirrors, particularly those with complex or freeform surfaces.

Although this work investigates the dynamics of a LOMP robot with joint friction, it does not account for time-varying effects. Given the extended duration of the LOMP cycle, prolonged and uninterrupted operation will inevitably lead to phenomena such as frictional wear and fatigue. Therefore, future research should account for time-varying parameters, such as the friction coefficient and link mass. This necessitates the development of online parameter identification algorithms or adaptive/robust control strategies to maintain high system performance in the presence of such parameter fluctuations.

Author Contributions: Conceptualization, Z.J. and H.L.; methodology, H.L.; software, Z.J.; validation, Z.J.; formal analysis, Z.J.; investigation, H.L.; resources, Z.J. and Z.Y.; data curation, H.L.; writing—original draft preparation, H.L.; writing—review and editing, Z.J.; visualization, H.L.; supervision, Z.Y.; project administration, H.L.; funding acquisition, Z.J., H.L. and Z.Y. All authors have read and agreed to the published version of the manuscript.

Funding: This research was funded by the Doctoral Scientific Research Foundation of Suzhou University, grant number 2023BSK016 (Z.J.); the Key Project of Natural Science Research in Universities of Anhui Province, grant number 2023AH052237 (H.L.) and 2024AH051812 (Z.J.); the Excellent Scientific Research and Innovation Teams in Anhui Province's Universities, grant number 2023AH010055 (Z.J., Z.Y.); the Key Research and Development Program Projects in Anhui Province, grant number 2023t070200 (Z.Y.); the Anhui Province Higher Education Provincial Quality Engineering Project, grant number 2023sdxx088 (Z.Y., Z.J.), 2024sx154 (Z.J.), and 2023cyts045 (Z.Y., Z.J.); and the Inland Visiting and Research Fellowship Program for Young Key Teachers, grant number JNFX2024063 (Z.Y.).

Data Availability Statement: Data are contained within the article.

Conflicts of Interest: The authors declare no conflicts of interest.

References

1. Sah, M.K.; Vijaya, A. Optimizing highly reflective CNC abrasive polishing on aluminum sheets. *Mater. Manuf. Process.* **2024**, *39*, 1144–1161. [CrossRef]
2. Su, C.X.; Li, B.; Zhang, W.; Tian, W.; Liao, W.H. An analysis and reliability-based optimization design method of trajectory accuracy for industrial robots considering parametric uncertainties. *Reliab. Eng. Syst. Saf.* **2024**, *254*, 110626. [CrossRef]
3. Plitea, N.; Szilaghyi, A.; Pisla, D. Kinematic analysis of a new 5-DOF modular parallel robot for brachytherapy. *Robot. Comput. -Integr. Manuf.* **2015**, *31*, 70–80. [CrossRef]
4. Jin, Z.; Yin, Z.; Liu, H.; Liu, F. Dynamic characteristics, analysis, and measurement of a large optical mirror processing system. *Machines* **2024**, *12*, 788. [CrossRef]
5. Fu, J.X.; Gao, F. Optimal design of a 3-Leg 6-DOF parallel manipulator for a specific workspace. *Chin. J. Mech. Eng.* **2016**, *29*, 659–668. [CrossRef]
6. Yang, K.; Yang, W.Y.; Wang, C.M. Inverse dynamic analysis and position error evaluation of the heavy-duty industrial robot with elastic joints: An efficient approach based on lie group. *Nonlinear Dyn.* **2018**, *92*, 487–504. [CrossRef]
7. Wang, X.; Peng, M.; Hu, Z.; Chen, Y.; Lin, Q. Feasibility investigation of large-scale model suspended by cable-driven parallel robot in hypersonic wind tunnel test. *Proc. Inst. Mech. Eng. Part. G-J. Aerosp. Eng.* **2017**, *231*, 2375–2383. [CrossRef]
8. Meng, D.S.; She, Y.; Xu, W.F.; Lu, W.F.; Liang, B. Dynamic modeling and vibration characteristics analysis of flexible-link and flexible-joint space manipulator. *Multibody Syst. Dyn.* **2018**, *43*, 321–347. [CrossRef]
9. Li, Y.; Bian, H.; Wang, L. Parameters identification and contact interaction control of redundant robot based on dynamic model. *Phys. Scr.* **2018**, *99*, 085270. [CrossRef]
10. Petrone, V.; Ferrentino, E.; Chiacchio, P. The dynamic model of the UR10 robot and its ROS2 integration. *IEEE Trans. Ind. Inform.* **2025**, *21*, 3828–3838. [CrossRef]
11. Pham, M.N.; Hazel, B.; Hamelin, P.; Liu, Z.H. Vibration control of flexible joint robots using a discrete-time two-stage controller based on time-varying input shaping and delay compensation. *J. Dyn. Syst. Meas. Control-Trans. ASME* **2021**, *143*, 101001. [CrossRef]
12. Yu, H.D.; Zhao, C.Z.; Zheng, H. A higher-order variable cross-section viscoelastic beam element via ANCF for kinematic and dynamic analyses of two-link flexible manipulators. *Int. J. Appl. Mech.* **2017**, *9*, 1750116. [CrossRef]
13. Kalani, H.; Rezaei, A.; Akbarzadeh, A. Improved general solution for the dynamic modeling of gough-stewart platform based on principle of virtual work. *Nonlinear Dyn.* **2016**, *83*, 2393–2418. [CrossRef]
14. Huang, Q.X.; Zhou, J.X.; Chen, X.; Yao, Y.X.; Chen, Y.H.; Chen, W.; Chen, R.J.; Lv, Z.S. Modeling and control of a two-axis stabilized gimbal based on kane method. *Sensors* **2024**, *24*, 3615. [CrossRef]
15. Chen, X.L.; Jia, Y.H.; Yu, D.; Wang, Q. Dynamics behavior analysis of parallel mechanism with joint clearance and flexible links. *Shock. Vib.* **2018**, *2018*, 9430267. [CrossRef]
16. Cheng, G.; Shan, X.L. Dynamics analysis of a parallel hip joint simulator with four degree of freedoms (3R1T). *Nonlinear Dyn.* **2012**, *70*, 2475–2486. [CrossRef]
17. Lang, D.; Song, Y.M.; Tao, T. Nonlinear dynamic modeling and performance analysis of a redundantly actuated parallel manipulator with multiple actuation modes based on FMD theory. *Nonlinear Dyn.* **2018**, *89*, 391–428. [CrossRef]

18. Chen, G.; Rui, X.; Abbas, L.K.; Wang, G.; Yang, F.; Zhu, W. A nocel method for the dynamic modeling of stewart parallel mechanism. *Mech. Mach. Theory* **2018**, *126*, 397–412. [CrossRef]
19. Danaei, B.; Arian, A.; Masouleh, M.T.; Kalhor, A. Dynamic modeling and base inertial parameters determination of a 2-DOF spherical parallel mechanism. *Multibody Syst. Dyn.* **2017**, *41*, 367–390. [CrossRef]
20. Hou, Y.; Wang, Y.; Jing, G.; Deng, Y.; Zeng, D.; Qiu, X. Chaos phenomenon and stability analysis of RU-RPR parallel mechanism with clearance and friction. *Adv. Mech. Eng.* **2018**, *10*, 1687814017746253. [CrossRef]
21. Jiang, L.J.; Gao, B.T.; Zhu, Z.Y. Dynamic modeling and control of a cable-driven parallel mechanism with a spring spine. *Proc. Inst. Mech. Eng. Part C-J. Mech. Eng. Sci.* **2017**, *231*, 3940–3958. [CrossRef]
22. Yang, J.; Xu, Z.; Wu, Q.; Zhu, M.; He, S.; Qin, C. Dynamic modeling and control of a 6-DOF micro-vibration simulator. *Mech. Mach. Theory* **2016**, *104*, 350–369. [CrossRef]
23. Wang, G.X.; Liu, H.Z.; Deng, P.S.; Yin, K.M.; Zhang, G.G. Dynamic analysis of 4-SPS/CU parallel mechanism considering three-dimensional wear of spherical joint with clearance. *J. Tribol. Trans. ASME* **2017**, *139*, 021608. [CrossRef]
24. Zhang, L.J.; Guo, F.; Li, Y.Q.; Lu, W.J. Global dynamic modeling of electro-hydraulic 3-UPS/S parallel stabilized platform by bond graph. *Chin. J. Mech. Eng.* **2016**, *29*, 1176–1185. [CrossRef]
25. Vaiedi-Koulaei, S.M.; Daniali, H.M.; Farajtabar, M.; Fathi, B.; Shafiee-Ashtiani, M. Reducing the undesirable effects of joints clearance on the behavior of the planar 3-RRR parallel manipulators. *Nonlinear Dyn.* **2016**, *86*, 1007–1022. [CrossRef]
26. Zhu, C.X.; Wang, J.; Chen, Z.W.; Liu, B. Dynamic characteristic parameters identification analysis of a parallel manipulator with flexible links. *J. Mech. Sci. Technol.* **2014**, *28*, 4833–4840. [CrossRef]
27. Van, M.; Mavrovouniotis, M.; Ge, S.S. An adaptive backstepping nonsingular fast terminal sliding mode control for robust fault tolerant control of robot manipulators. *IEEE Trans. Syst. Man Cybern. Syst.* **2018**, *49*, 1448–1458. [CrossRef]
28. Wu, Q.C.; Wang, X.S.; Chen, B.; Wu, H.T.; Shao, Z.Y. Development and hybrid force/position control of a compliant rescue manipulator. *Mechatronics* **2017**, *46*, 143–153. [CrossRef]
29. Nair, R.R.; Behera, L.; Kumar, S. Event-Triggered Finite-Time integral sliding mode controller for Consensus-Based formation of multirobot systems with disturbances. *IEEE Trans. Control. Syst. Technol.* **2019**, *27*, 39–47. [CrossRef]
30. Prinz, K.; Steinboeck, A.; Muller, M.; Ettl, A.; Kugi, A. Automatic gauge control under laterally asymmetric rolling conditions combined with feedforward. *IEEE Trans. Ind. Appl.* **2017**, *53*, 2560–2568. [CrossRef]
31. Mao, X.F.; Wang, Y.J.; Liu, X.D.; Guo, Y.G. A hybrid Feedforward-Feedback hysteresis compensator in piezoelectric actuators based on Least-Squares support vector machine. *IEEE Trans. Ind. Electron.* **2018**, *65*, 5704–5711. [CrossRef]

Disclaimer/Publisher's Note: The statements, opinions and data contained in all publications are solely those of the individual author(s) and contributor(s) and not of MDPI and/or the editor(s). MDPI and/or the editor(s) disclaim responsibility for any injury to people or property resulting from any ideas, methods, instructions or products referred to in the content.